Influence of the geometry of stemless implants on the bone adaptation process of the humerus: a computational analysis

Manuel Rosado Nunes Comenda[1]

Instituto Superior Técnico, Lisbon, Portugal
[1]e-mail: manuel.comenda@tecnico.ulisboa.pt

ABSTRACT

Aiming to reduce stem-related complications of the shoulder arthroplasty, a new type of implants arose, the stemless implants. Despite the good results in clinical studies, there is a lack of knowledge about the influence of these implants at long-term, critical to the success of the procedure, especially considering the differences in the geometry of the commercialized implants. The goal of this study was to analyse the influence of the geometry of 5 stemless implants on the bone adaptation process of the humerus after a shoulder arthroplasty. To accomplish that, shoulder arthroplasties were virtually simulated in Solidworks®, and three-dimensional finite element models were developed in Abaqus® to be used with a bone remodelling model. The analysed models were based on the ECLIPSE™ Stemless Shoulder Prosthesis from Arthrex, GLOBAL ICON™ Stemless Shoulder System from DePuy Synthes, SMR® Stemless from Lima Corporate, SIMPLICITI™ Shoulder System from Wright, and Sidus™ Stem-Free Shoulder from Zimmer. For the validation of the bone remodelling model, its bone remodelling parameters were adjusted to allow the simulation of the actual humerus density distribution. The simulations for the bone-implant assemblies were performed using those parameters. The analysis of the results was performed qualitatively, by evaluating the absolute changes in bone density with respect to the intact bone and, quantitatively, by computing the changes in bone mass for different regions of interest. Overall, the results obtained show that the differences in the implants' geometry influence the bone adaption process. From the bone remodelling point of view, the Global Icon, SMR, and Simpliciti implant showed a good performance, whereas the Eclipse implant had the worst performance, followed by the Sidus implant.

Keywords: Humerus, Shoulder Arthroplasty, Stemless implants, Bone remodelling, Finite element method.

1. Introduction

According to Lübbeke et al. (2017), annual incidence rates of shoulder arthroplasty have nearly tripled over the last decade and, although shoulder arthroplasty is seen as a satisfactory treatment for the rheumatoid or osteoarthritic glenohumeral joint, its long-term performance still presents some concerns. For instance, the stress shielding effect, characterized by an adaptation of bone to changes in load distribution due to the insertion of an implant into the bone, according to Wolff's law, may be the cause of several complications. These remodelling processes weaken the bone, either making it thinner or more porous, and subsequently increasing the risk of implant failure and periprosthetic fractures.

Since the first report of a shoulder arthroplasty, there is a trend of shortening the stem's length of the humeral components to avoid stem-related complications, such as periprosthetic fractures and the occurrence of the stress shielding effect. Consequently, the last generation of shoulder implants consists in stemless implants. Besides intending to reduce the stem-related concerns, these implants allow an easier surgical procedure by reducing the surgical steps, the blood loss and the mean operative time (Berth & Pap, 2013). Additionally, this type of implants preserve proximal bone stock, which is critical for a future revision surgery, if needed, especially considering the increase of a younger population needing surgery (Nagels et al., 2003). An optimal glenoid exposure is also beneficial when compared to humeral resurfacing implants (Churchill & Athwal, 2016).

There is an increase in clinical trials addressing the performance of stemless implants, for which functional and radiologic clinical outcomes are promising and comparable to those of standard stemmed implants, either in short, mid or long-term follow-ups (Hawi et al., 2017). Nevertheless, there is evidence of the prevalence of complications, as reported by Habermeyer et al. (2015), who observed a lowering of density of cancellous bone in the proximal humerus in 41.3 % of the patients. More recently, a study presenting clinical and radiologic outcomes after 9 years of follow-up also reported a lowering of bone mineral density in radiographs of the humerus in 29.4 % of patients (Hawi et al., 2017). Regarding computational analyses, only a few finite element studies address the performance of stemless implants. In 2015, Razfar et al. (2015) used a three-dimensional finite element analysis to evaluate the effect of humeral component length

on stresses in the proximal humerus, including in his study one generic model of a stemless implant. Later, using three-dimensional finite element models, Favre & Henderson (2016) investigated the micromotion of one stemless humeral implant model, based on a commercialized implant, during several daily routine activities. More recently, Reeves et al. (2018) used several generic three-dimensional finite element models of stemless implants to study the effect of implant geometry on the simulated stress and strain response of the proximal humerus. Moreover, Santos et al. (2018) addressed the bone remodelling process of the humerus after the introduction of one stemless implant model based on a commercialized implant, also using three-dimensional finite element models.

The present study is motivated by the prevalence of complications in the stemless shoulder arthroplasty, and by the lack of knowledge regarding the influence of these implants on the long-term outcome of the procedure, especially considering the significant geometry variability of the available implants, which prevents extrapolation of the outcome of one implant to the others. The goal of the present work is to analyse the impact of 5 geometries of stemless implants, available in the market, on the bone adaptation process of the humerus, using three-dimensional finite element models.

2. Methods

Finite element model

A three-dimensional, 3-D, model of the right humerus was obtained by the segmentation of computed tomography, CT, scan images from a 38-years-old male cadaver, acquired by the Visible Human Project (Spitzer et al., 1996). For the sake of brevity, a sample of 5 stemless shoulder arthroplasty implants were modelled using the commercial software Solidworks® (Student Edition, Academic Year 2016-2017). Within this sample, all the implants geometries have a significant variability which is believed to give an insight about the geometries commercialized. These models were based on the ECLIPSE™ Stemless Shoulder Prosthesis from Arthrex, GLOBAL ICON™ Stemless Shoulder System from DePuy Synthes, SMR® Stemless from Lima Corporate, SIMPLICITI™ Shoulder System from Wright and Sidus™ Stem-Free Shoulder from Zimmer. Henceforth, these implants will be referred as Eclipse, Global Icon, SMR, Simpliciti and Sidus, respectively. The shoulder arthroplasties, illustrated in Figure 1, were virtually simulated in Solidworks®.

From the 3-D geometric models, 6 finite element models were created in Abaqus® (version 2017, 2016), using linear tetrahedral meshes, corresponding to the intact model of the humerus and the humerus with the 5 implants models, hereafter referred to as intact bone model and implanted models, respectively.

The implants models were modelled as a linear elastic, homogeneous, and isotropic materials, considering values for the modulus of elasticity of 230 GPa and 115 GPa for the heads of the implants (chromium cobalt alloy) and for the metaphyseal components (titanium alloy), respectively. The bone was modelled as a linear elastic material with an orthotropic microstructure. Its material properties are obtained through the bone remodelling process assuming a Young's modulus of 17.5 GPa for cortical bone. For all components, a Poisson's coefficient of 0.3 was used (Gupta & Dan, 2004; Quental et al., 2012b).

The interactions between bone and the coated or blasted regions of the different components of the implants were modelled considering an ideal condition, for which full osseointegration occurred, and a worst-case condition, for which no osseointegration occurred. For the ideal condition, interactions between bone and the coated or blasted surfaces, highlighted in green in Figure 1, were defined as bonded using a tie constraint (Dassault Systèmes, 2015). For the worst-case condition, a contact formulation was considered instead (Dassault Systèmes, 2015). The friction coefficients used are listed in Table 1. For the Global Icon and Sidus models, the friction coefficient was assumed to be 0.6 because no additional information was found regarding the type of rough titanium coating applied.

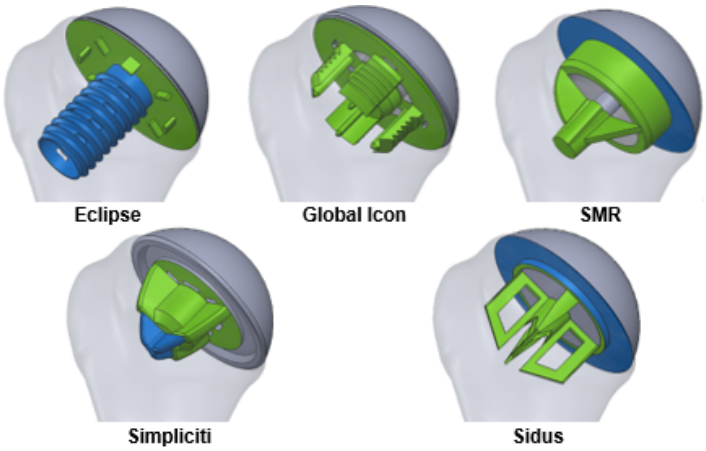

Figure 1 - Anterior view of the interactions between the bone and the implant for all 5 models. The surfaces highlighted in green and blue represent, respectively, a bonded contact (tie constraint) and a frictional contact (penalty formulation).

Excluding one case, all interactions between the different components of each implant were considered bonded through a tie condition. Both undersurfaces of the SMR and Sidus humeral heads are in contact with the resection surface of the bone, being modelled as frictional contact with a penalty frictional formulation. The interactions between the Eclipse cage screw and bone, the Simpliciti nucleus' bottom and bone, the undersurface of the Eclipse humeral head and the upper surface of the trunion (Magosch et al., 2012), and the upper lateral surface of the Sidus' anchor and bone were also simulated using a contact formulation. All contact interactions are highlighted in blue in Figure 1.

In this study, 6 load cases, related to 10º, 60º and 90º positions of abduction in the coronal plane and anterior flexion in the sagittal plane, were considered (Santos et al., 2018).

Table 1 – Friction coefficients applied for the different interactions considered in the finite element models developed.

Materials	Coefficients of Friction
Bone – Titanium Plasma Spray (Eclipse's trunion undersurface)	0.6 (Grant et al., 2007)
Bone – Trabecular Titanium (SMR's core component)	2.2 (Lima Corporate, 2016)
Bone - Sintered Titanium Beads (Upper part of Simpliciti's nucleus)	0.53 (Rancourt & Drouin, 1990)
Bone – Chromium-Cobalt	0.26 (Sobocinski, 2015)
Bone - Titanium	0.36 (Eberle & Augat, 2007)
Titanium - Chromium-Cobalt	0.3 (Swaminathan & Gilbert, 2012)

Each load case includes the glenohumeral reaction force and the action of 11 muscles. The load applied to the humerus was estimated by an inverse dynamic analysis of a multibody musculoskeletal model of the upper limb composed of 7 rigid bodies, 6 anatomical joints, and 21 muscles (Quental et al., 2012a). The muscle attachment sites are illustrated in Figure 2. To prevent rigid body motion, the humerus was fixed at its lower extremity with an encastre condition, restricting all displacements and rotations (Dassault Systèmes, 2015) as shown in Figure 2.

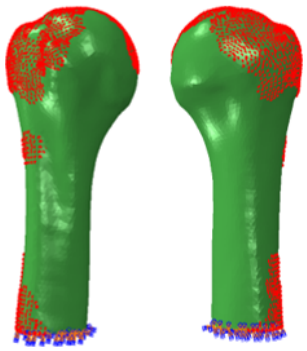

(a) (b)

Figure 2 - Anterior (a) and posterior (b) view of the intact model. The nodes in red represent the regions where load is applied. It includes all the regions correspondent to action of the 11 muscles, as well as the glenohumeral joint reaction force, for all the load cases. It is also represented the encastre condition in the lower extremity of the model.

Bone remodelling model

The bone remodelling model used in this work was developed by Fernandes et al. (1999). It assumes trabecular bone as a cellular material, with its microstructure being modelled as the periodic repetition of a unit cell. In this study, the configuration of the unit cell is cubic with throughout rectangular holes. For each point within the body, the microstructure is characterized by its relative density and orientation, computed through the parameters $\mathbf{a}$ and Euler angles $\boldsymbol{\theta}$, respectively (Folgado et al., 2004; Quental et al., 2014b). As the modelled cellular material is orthotropic, it allows the simulation of bone as an oriented material. The bone remodelling process consists in an optimization problem that minimizes the structural compliance, i.e., maximizes the structural stiffness. The objective function to be minimized considers a biological term associated to the cost of bone maintenance. This term is controlled by the parameter k, which represents the metabolic cost to the organism of maintaining bone tissue. The stationary conditions of the optimization problem with respect to the design variables $\mathbf{a}$ and $\boldsymbol{\theta}$ yield the bone remodelling law, mathematically expressed as:

$$\sum_{P=1}^{NC}\left(\alpha^{P}\frac{\partial \mathrm{E}^{\mathrm{H}}_{ijkl}}{\partial \mathbf{a}}\varepsilon_{ij}\varepsilon_{kl}\right)-k\frac{\partial\left(\rho_r^{m}\right)}{\partial \mathbf{a}}=0 \qquad (2\text{-}1)$$

$$\sum_{P=1}^{NC}\left(\alpha^{P}\frac{\partial \mathrm{E}^{\mathrm{H}}_{ijkl}}{\partial \boldsymbol{\theta}}\varepsilon_{ij}\varepsilon_{kl}\right)=0 \qquad (2\text{-}2)$$

where NC is the number of applied load conditions with the load weight factors α^{P}, satisfying $\sum_{P=1}^{NC}\alpha^{P}=1$. The variable $\boldsymbol{\varepsilon}$ is the strain field, and $\mathrm{E}^{\mathrm{H}}_{ijkl}$ are the homogenized bone material properties (Guedes & Kikuchi, 1990). The variable ρ_r is the relative density, and the parameter m represents a corrective factor for the preservation of intermediate densities (Folgado, 2004). Given the initial parameters $\mathbf{a_0}$ and $\boldsymbol{\theta_0}$, the homogenized elastic properties are computed using the homogenization method. Then, the finite element method is applied to compute the displacement field, which is followed by a check of the stationary conditions. If these conditions, represented by the Equations (2-1) and (2-2), are satisfied, the bone is in equilibrium and the process stops. If they are not satisfied the process continues by updating the parameters $\mathbf{a}$ and $\boldsymbol{\theta}$. The load weight factors α^{P}, described in Equations (2-1) and (2-2), were calculated according to the relative frequencies of arm movements during daily activities. For the arm elevation angles of 10°, 60° and 90°, the weight factors are 0.251371, 0.055667 and 0.011659 for abduction, and 0.537375, 0.119003 and 0.024924 for flexion, respectively (Coley et al., 2008, 2009). A node-based approach (Jacobs et al., 1995) were followed for the bone remodelling simulations.

Validation of the bone remodelling model

Before applying the bone remodelling model to the 5 bone-implant assemblies, simulations of the intact bone model were performed to validate the application of the bone remodelling model. The goal was to assess if the model could successfully reproduce the actual bone density distribution of the humerus under analysis. For that purpose, different simulations were performed considering 8 values for the parameter k, ranging from 1×10^{-5} to 3.5×10^{-4}, and 5 values for the parameter m ranging from 1 to 5. For the sake of comparison, all simulations were run for 200 iterations.

Using bonemapy (version 0.4.1, 2013), an Abaqus® freeware plug-in (Hogg, 2013), and the calibration procedure described by Gupta & Dan (2004), the actual bone density distribution of the humerus was estimated from the CT scan images, used to create the 3-D geometry of the bone.

Qualitative and quantitative analyses were performed to assess which set of bone remodelling model parameters best reproduced the actual bone density distribution of the humerus being studied. On one hand, the results were visually compared with the CT scan images and, on the other hand, a statistical analysis was performed to compare the predicted bone densities with those from the CT scan images. For that purpose, the root-mean-square error, RMSE, (based on relative $\Delta\rho_r$ and absolute $\Delta\rho_a$ differences), mean, standard deviation, SD, (Quental et al., 2014b), and the mean error, ME, between the densities of the bone remodelling simulations and the CT scan images were computed for each simulation. Notice that the RMSE computed here weighed each node i by its volume V_i, i.e.:

$$\mathrm{RMSE} = \sqrt{\frac{\sum_{i=1}^{n}(\Delta\rho_i \times V_i)^2}{\sum_{i=1}^{n} V_i}} \qquad (2\text{-}3)$$

where n denotes the total number of nodes to be evaluated and $\Delta\rho_i$ is the density difference for each node i. The ME is mathematically expressed as:

$$\mathrm{ME}(\%) = \frac{\bar{x}_{BR} - \bar{x}_{CT}}{\bar{x}_{CT}} \times 100 \qquad (2\text{-}4)$$

where the variables $\bar{x}_{BR}$ and $\bar{x}_{CT}$ are the mean density of the humeral head at the end of the bone remodelling simulation and in the CT scan images, respectively. The region analysed was the humeral head, above the surgical neck, since it is the major region of interest given the implants' geometry.

Bone remodelling simulations after the virtual shoulder arthroplasty

The bone remodelling simulations for the implanted models were performed for a fully osseointegration condition and a fully absent osseointegration condition, considering the parameters k and m selected in the validation step, which were deemed as the best to reproduce the actual bone density distribution of the bone under analysis. All simulations were performed for 200 iterations. The initial condition was defined as the bone density distribution obtained for the intact bone model, after 200 iterations using the set of parameters selected as best.

To remove possible numerical factors from the analysis of the results, the bone remodelling simulations after a shoulder arthroplasty were compared to the bone density distribution of the intact bone obtained for 400 iterations. Figure 3 illustrates, and summarizes, the methodology adopted.

The analysis of the results was performed qualitatively, by evaluating the absolute changes in bone density with respect to the intact bone and, quantitatively, by computing the changes in bone mass for different 8 proximal regions of the humerus, defined based on Reeves et al. (2017). The bone is divided into anterior, posterior, medial and lateral sections, and each of these sections is divided into superficial and deep sections by a transversal plane. Figure 4 presents a scheme of the regions of interest, ROI, described.

The change in bone mass is mathematically expressed as:

$$\Delta bm(\%) = \frac{\sum_{i=1}^{n}\left(\rho_i^{2ooWI} - \rho_i^{400WOI}\right) \times V_i}{\sum_{i=1}^{n} \rho_i^{200WOI} \times V_i} \times 100 \qquad (2\text{-}5)$$

where n is the total number of nodes within the ROI under analysis, V_i is the volume associated to each node i, ρ_i^{2ooWI} is the density of node i $(i \in R\,O\,I)$ for the implanted model at the

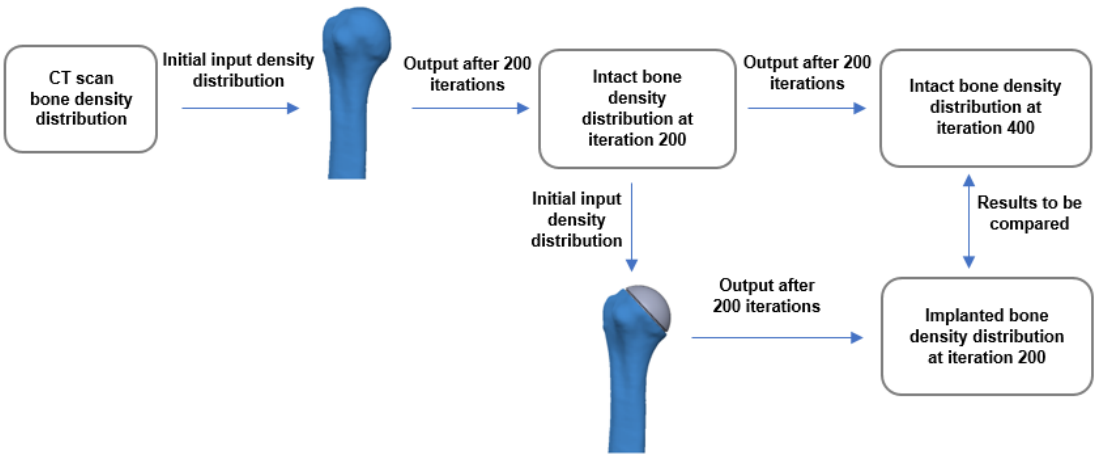

Figure 3 – Illustration of the bone material properties during the bone remodelling simulations.

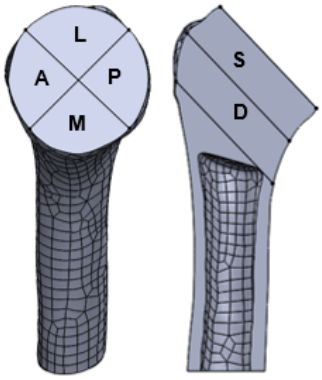

(a) (b)

Figure 4 - (a) A, L, P, and M represent, respectively, the regions of interest anterior, lateral, posterior and medial. (b) Anterior view of transversal division: S, superficial ROI; D, deep ROI.

end of the bone remodelling simulation, and ρ_i^{200WOI} and ρ_i^{400WOI} are the densities of node i $(i \in ROI)$ for the intact bone model at the iterations 200 and 400, respectively.

To assess the amount of mass removed by each implant during the surgical procedure, the overall change in bone mass was computed with respect to the stage before the virtual arthroplasty.

To analyse the sensitivity of the results on parameter k, additional simulations were performed considering parameters k 50 % larger and 50 % smaller than that deemed as best. The parameter m remained constant in this sensitivity analysis.

3. Results

Validation of the bone remodelling model

Bone remodelling simulations were performed for 200 iterations ensuring that the average change in bone density between consecutive iterations was below 1×10^{-3} g cm^{-3} at the end of each simulation. The evaluated values were 1×10^{-5}, 5×10^{-5}, 1×10^{-4}, 1.5×10^{-4}, 2×10^{-4}, 2.5×10^{-4}, 3×10^{-4} and 3.5×10^{-4} for the parameter k, and 1, 2, 3, 4 and 5 for the parameter m. The RMSE, mean, SD, and ME between the densities of the bone remodelling simulations and the CT scan images computed for each simulation are presented in detail in Table 2. For the sake of comparison, the RMSEs were normalized by the maximum RMSE value obtained for each difference, so that it is dimensionless and, at most, unitary. For brevity, only the results for the analyses with parameter m of 1, 2 and 3 are presented.

The lowest RMSEs were obtained for a parameter k of 1.5×10^{-4} and a parameter m of 2 for the absolute difference, and a parameter k of 2.5×10^{-4} and a parameter m of 2, for the relative difference. However, the solution characterized by the parameter k of 1.5×10^{-4} and the parameter m of 2 has the lowest mean error, meaning that its average density distribution in the humeral head is more similar to the actual bone density distribution than the solution of the parameter k of 2.5×10^{-4} and the parameter m of 2. Accordingly, the solution for the parameter k of 1.5×10^{-4} and the parameter m of 2 is deemed as the best to reproduce the actual bone density distribution of the humerus under analysis.

Table 2 – Normalized RMSEs based on $\Delta\rho_a$ and $\Delta\rho_r$ between the density of the bone remodelling simulations and the CT scan images, mean and SD of the performed bone remodelling simulations, and the error between the mean of the bone density distribution, for each simulation, with the mean of actual bone density distribution. The RMSEs presented for $\Delta\rho_a$ and $\Delta\rho_r$ are normalized by the maximum RMSE value obtained for each difference, i.e., 0.0247 g cm$^{-\frac{3}{2}}$ and 0.0507 cm$^{\frac{3}{2}}$, respectively.

m	k	RMSE		Mean (SD) g cm^{-3}	ME (%)
		$\Delta\rho_a$	$\Delta\rho_r$		
1	1×10^{-5}	0.8374	0.8749	0.7582 (0.3681)	46.32
	5×10^{-5}	0.6641	0.6665	0.6356 (0.3686)	22.67
	1×10^{-4}	0.6167	0.6367	0.5106 (0.3609)	1.45
	1.5×10^{-4}	0.6857	0.7248	0.4154 (0.3490)	19.83
	2×10^{-4}	0.7827	0.8227	0.3442 (0.3360)	33.57
	2.5×10^{-4}	0.8717	0.9015	0.2911 (0.3233)	43.82
	3×10^{-4}	0.9437	0.9588	0.2516 (0.3111)	51.44
	3.5×10^{-4}	1.0000	1.0000	0.2219 (0.3000)	57.17
2	1×10^{-5}	0.8426	0.9009	0.7643 (0.3568)	47.51
	5×10^{-5}	0.6641	0.6665	0.6356 (0.3686)	22.67
	1×10^{-4}	0.5643	0.6062	0.5766 (0.2835)	11.28
	1.5×10^{-4}	0.5421	0.5512	0.5118 (0.2568)	1.23
	2×10^{-4}	0.5567	0.5330	0.4655 (0.2375)	10.17
	2.5×10^{-4}	0.5821	0.5313	0.4313 (0.2233)	16.77
	3×10^{-4}	0.6081	0.5355	0.4051 (0.2126)	21.82
	3.5×10^{-4}	0.6318	0.5414	0.3842 (0.2041)	25.85
3	1×10^{-5}	0.8553	0.9221	0.7714 (0.3533)	48.86
	5×10^{-5}	0.7214	0.8191	0.7014 (0.3075)	35.35
	1×10^{-4}	0.6290	0.7439	0.6385 (0.2665)	23.21
	1.5×10^{-4}	0.5881	0.7058	0.5960 (0.2399)	15.01
	2×10^{-4}	0.5715	0.6851	0.5660 (0.2224)	9.24
	2.5×10^{-4}	0.5654	0.6717	0.5436 (0.2102)	4.91
	3×10^{-4}	0.5638	0.6610	0.5259 (0.2012)	1.48
	3.5×10^{-4}	0.5640	0.6512	0.5111 (0.1941)	1.37

For a qualitative analysis of the results, Figure 5 compares the bone density distribution obtained computationally with that of the CT scan images. For the sake of briefness, only 3 slices are shown. Despite differences existing between the computational predictions and the CT scan images, the bone density distributions are generally comparable.

Bone remodelling simulations after the virtual shoulder arthroplasty

For the sake of comparison, all simulations were run for 200 iterations. The average change in bone density was

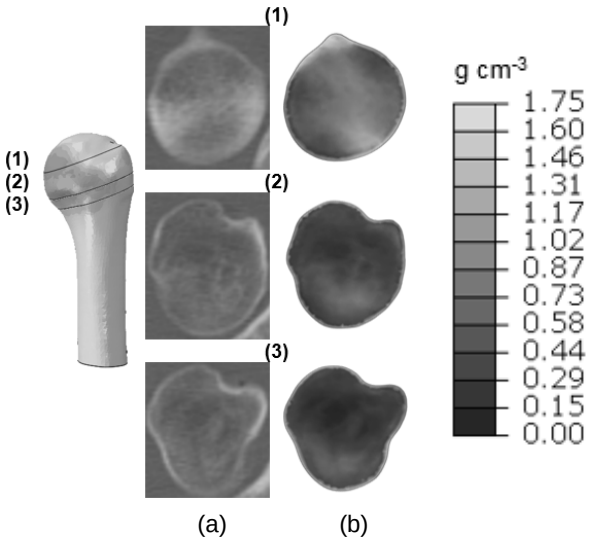

Figure 5 – Comparison between the CT scan images (a) and the bone remodelling result (bone density) (b) for the selected parameters k and m, 1.5×10^{-4} and 2, respectively.

always below 1×10^{-3} g cm^{-3} at the end of all simulations. Figure 6 presents the absolute changes in bone density computed for each implanted bone with respect to the intact bone. For the sake of simplicity, negative changes in bone density were classified as bone resorption, while positive changes were classified as bone apposition. The equilibrium condition, depicted in green, is defined for an absolute change, $\Delta\rho$, in bone density below 0.1 g cm^{-3} (-0.1 g cm^{-3} $< \Delta_\rho <$ 0.1 g cm^{-3}). Both bone resorption and bone apposition were divided into two levels. Bone resorption is depicted in red ($\Delta_\rho < -0.2$ g cm^{-3}) and orange (-0.2 g cm^{-3} $\leq \Delta_\rho \leq -0.1$ g cm^{-3}), whereas bone apposition is depicted in dark blue ($\Delta_\rho > 0.2$ g cm^{-3}) and light blue (0.1 g cm^{-3} $\leq \Delta_\rho \leq$ 0.2 g cm^{-3}).

Table 3 presents in detail the changes in bone mass for each ROI and each implant. Negative values reflect bone mass loss whereas positive values reflect bone mass gain. For consistency, the colour code used refers to bone adaption phenomena such as bone resorption, bone apposition and equilibrium condition according to Figure 6. However, the equilibrium condition was arbitrarily defined for a change in bone mass below 5 %, and the boundary of the remaining level was arbitrarily defined for a change in bone mass of 10 %.

Overall, the bone mass loss was more pronounced in the superficial ROIs. The Eclipse model showed the higher amount of bone mass loss in all the humeral head region, followed by the Sidus model. The Global Icon and SMR models presented a more moderated bone mass loss, and the Simpliciti implant was the only implant to cause an increase in bone mass in all the humeral head region. The region covered by the solid collar of the Eclipse, Global Icon, and Simpliciti implants showed bone resorption, as well as the superficial, anteromedial region of the resected humerus, in the Sidus model. The SMR implant caused very little bone resorption. Bone formation is mostly observed in the regions around the implants' fins of all 5 implants, and in the interfaces between the resected surface of the humerus and the undersurface of the humeral heads of the SMR and Sidus implants.

The change in bone mass due to the virtual shoulder arthroplasty and the posterior bone adaptation process is graphically represented in Figure 7. The stages considered were the stage before the arthroplasty, 0^-, the stage immediately after the arthroplasty, 0^+, and the stage in the end of the bone remodelling simulation, 1, after the adaptation of bone to the implant.

The SMR implant is the implant that removed the largest amount of bone mass during the arthroplasty, whereas the Eclipse is the implant that removed less bone mass.

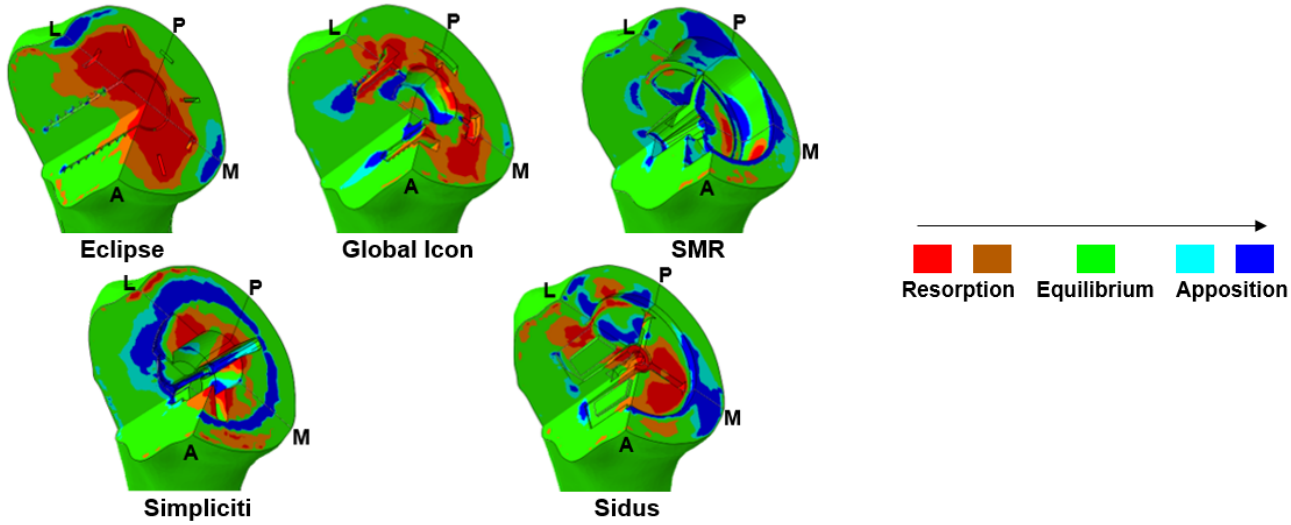

Figure 6 – Absolute changes, $\Delta\rho$, in bone density with respect to the intact bone, considering parameters k and m of 1.5×10^{-4} and 2, respectively. The legend L, P, M and A refers to the anatomical terms lateral, posterior, medial and anterior, respectively. The green color represents an equilibrium condition (-0.1 g cm^{-3} $< \Delta_\rho <$ 0.1 g cm^{-3}). Bone resorption condition is depicted in red ($\Delta_\rho < -0.2$ g cm^{-3}) and orange (-0.2 g cm^{-3} $\leq \Delta_\rho \leq -0.1$ g cm^{-3}). Bone apposition is depicted in dark ($\Delta_\rho > 0.2$ g cm^{-3}) and light blue (0.1 g cm^{-3} $\leq \Delta_\rho \leq$ 0.2 g cm^{-3}).

Despite the Eclipse implant being the implant that caused the largest bone mass loss during the bone adaption process, it is the SMR model that presented the lowest bone mass. Yet, it is worth noticing that the change in bone mass due to the bone adaptation process caused by the SMR implant was only 0.7 %.

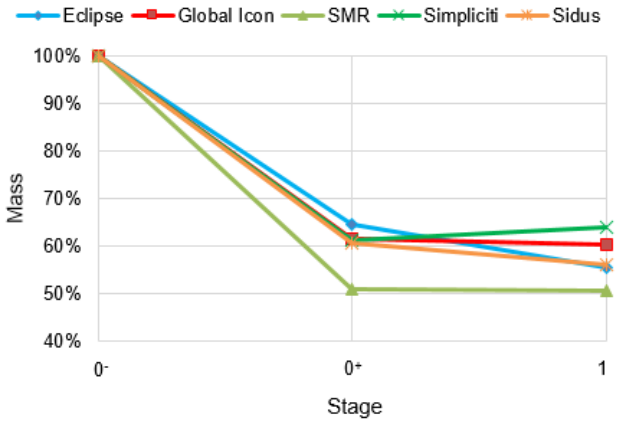

Figure 7 – Percentage of bone mass in three distinct stages: 0^- denotes the humeral head mass before the arthroplasty, 0^+ represents the mass of humeral head immediately after the arthroplasty, and 1 denotes the humeral head mass, after the adaptation of bone to the implant.

Overall, for the fully absent osseointegration condition, there is a general increase in bone apposition and a decrease in bone resorption. Nevertheless, the findings from the full osseointegration condition remain, as the relationship among the 5 implant models does not change. Therefore, these results are not presented here.

Regarding the sensitivity analysis, 2 values for the parameter k were evaluated. The parameters k of 0.75×10^{-4} and 2.25×10^{-4} are 50 % smaller and 50 % larger, respectively, than those deemed as best. The results showed that a decrease in the parameter k led to a decrease in bone resorption and an increase in bone apposition, whereas an increase in the parameter k leads to an increase in bone resorption and a decrease in bone apposition. Nonetheless, despite the quantitative changes in bone mass, no relevant differences were observed qualitatively, i.e., all 5 models maintained their relative performances.

4. Discussion

The objective of this study was to assess to what extent the bone adaptation process of the proximal humerus is affected by the distinct geometries of 5 stemless implants, available in the market. To accomplish that, 3-D finite element models of the stemless implants were applied along with a bone adaption model. The bone remodelling simulations were performed using the parameters selected in the bone remodelling model validation step, which were deemed as the best to simulate the actual humerus density distribution. The parameters selected as best presented low RMSE and ME between the computational predictions and the actual bone density distribution of the humerus under analysis, which provides confidence on the results. For the implanted bone models, the initial condition was defined as the bone density distribution obtained for the intact bone model using the set of parameters selected as best. The analysis of the results was performed qualitatively, by visually comparing the absolute changes in bone density with respect to the intact bone and, quantitatively, by computing the changes in bone mass for different ROI. Overall, the results obtained show that the differences in the implants' geometry influence the bone adaption process.

Overall, the Eclipse model presented the highest total bone mass loss, followed by the Sidus model, whereas the Global Icon and SMR models presented a moderate bone mass loss. The Simpliciti model stood out from the rest as it was the only one leading to an increase in total bone mass. The results obtained in this work show a great change in bone mass in the anterior superficial region, as well as relevant changes in the lateral superficial region of the proximal humerus. Apart from the changes in bone mass due to bone adaptation, it is worth noticing that the SMR implant is the one that removes more mass during its implantation, as opposed to the Eclipse model, which is the implant that preserves more bone. Global Icon, SMR, and Simpliciti implants showed a good performance. However, although the SMR model removes more bone mass, it is the one that shows the less

Table 3 – Changes in bone mass, in percentage, for each ROI with respect to the intact bone, considering k and m parameters of 1.5×10^{-4} and 2, respectively. The colour code refers to Figure 6. However, the equilibrium condition was arbitrarily defined for a change in bone mass below 5 %, and the boundary of the remaining level was arbitrarily defined for a change in bone mass of 10 %.

ROI		Eclipse		Global Icon		SMR		Simpliciti		Sidus	
S	L	-20.03	-17.48	-3.11	-6.85	-4.50	-1.87	7.44	0.65	-16.57	-11.83
	P	-7.79		-7.49		10.51		1.76		-1.69	
	M	-9.58		-8.82		-0.57		-2.82		-8.10	
	A	-28.53		-9.45		-8.45		-4.76		-22.82	
D	L	-8.70	-8.72	15.81	4.92	1.49	0.55	23.46	9.76	-7.67	-2.54
	P	0.92		-3.69		5.94		6.89		7.59	
	M	-5.72		0.87		-0.40		8.33		-0.76	
	A	-19.27		7.69		-2.22		1.26		-11.06	
Total		-13.93		-1.81		-0.67		4.54		-7.84	

impact on the bone remodelling of the humerus showing very little bone resorption. From the bone adaption process point of view, the superior bone resorption level predicted for the Global Icon and Simpliciti models at the superficial central region of the implant's fixation might suggest a better long-term performance of the SMR, even regardless of the gain in bone mass predicted for the Simpliciti implant, because the bone loss observed for the former implants could lead to loosening over time (Quental et al., 2014a; Reeves et al., 2018). Nevertheless, further investigation focusing on the long-term implant stability could give a better understanding on whether preserving bone stock should be preferred, despite bone resorption might occurring, over removing more bone stock during the surgical procedure, but avoiding bone resorption. For the fully absent osseointegration condition, there was a general increase in bone apposition and a decrease in bone resorption. Nevertheless, the findings from the full osseointegration condition remained, as the relationship among the 5 implant models did not change.

Regarding the influence of the collar type on the bone adaption process, for the 3 implants that present a solid collar (Eclipse, Global Icon, and Simpliciti), bone resorption occurred in the superficial, central region of the resected humerus, which is covered by the collar. This might be explained by the stress shielding phenomenon, i.e., the loads are transferred through the implant, causing a decrease in the mechanical stimulus in the bone that leads to bone resorption. Previous mid-term radiologic results about the Eclipse implant also showed bone mass loss and occurrence of stress shielding in this region (Habermeyer et al., 2015; Heuberer et al., 2018). Churchill & Athwal (2016) suggested that in the case of stress shielding and bone resorption occurring, collared implants may provide more stability contrarily to collarless implants. However, the bone loss observed in this study for the collared implants, at the superficial central region of the implant's fixation under the collar, could lead to implant loosening (Quental et al., 2014a). Therefore, further computational investigation should assess the long-term stability of stemless implants. Nevertheless, the short, mid and long-term radiologic studies about stemless implants report no loosening of the humeral component due to stress shielding (Habermeyer et al., 2015; Churchill et al., 2016; Hawi et al., 2017; Heuberer et al., 2018). Bone formation in the superficial region of the resected humerus was observed for the Simpliciti model at the edge of the solid collar. Its solid collar rests on the trabecular bone inside the cortical rim, instead of resting on the cortical rim. This type of solid collar might be advantageous as it allows a better transfer of loads to the metaphyseal region. The 2 implants that do not have a solid collar allow the contact between the humeral head component and the resected bone surface, which allows the transfer of load through these regions, and thus leads to bone apposition. The bone resorption in the superficial region of the Sidus model may be due to the open collar as no load is transferred to this region. The SMR implant is collarless and very little bone resorption occurred in the superficial region. Yet, notice that no bone stock exists inside the core. Because there is only one collarless implant model and one implant model with an open collar, no definite conclusions can be taken about these types of collars.

With respect to the fixation mode, the Eclipse implant is fixed by screw-in in the central region of the resected humerus, while the remaining 4 implants are impacted into the bone. The Global Icon implant is fixed through impaction with 4 peripheral legs and one central protuberance, the Sidus implant through 4 cross shaped open-windowed fins, and the Simpliciti and SMR implants through a central body with 3 fins that avoid the implant rotation. Unfortunately, since only one implant fixed by screw-in was analysed, no definite recommendations can be made regarding the fixation mode. Comparing the fixation features of the 4 implants fixed by impaction, the Sidus model showed a bone loss superior than that observed for the Simpliciti, Global Icon, and SMR models. However, this cannot be directly linked to the amount and shape of fins because other distinct features, such as the fixation position, might have played a role as well. According to Reeves et al. (2017) and Alidousti et al. (2017), the average apparent density in the proximal humerus decreases from the superficial to deep regions, and increases from the central to peripheral regions. Therefore, to seek fixation in a denser region, the design of the stemless implants should take advantage of the peripheral regions within the first 15-20 mm beneath the humeral head resection surface. Among these 4 implants, the Sidus implant is the system whose fins cover a more central region.

To the author's knowledge, there are no other FE studies addressing the effect of the geometry of distinct stemless implants, available in the market, in the bone remodelling process of the humerus. Reeves et al. (2018) addressed the effect of stemless humeral component fixation feature design on bone stress and strain response considering generic stemless implants. The implants analysed were classified according to the fixation feature location: central, peripheral, and boundary-crossing (when the central-peripheral boundary is crossed). Among others, one variable measured was the simulated potential bone response at the stage immediately after surgery, computed by the percentage of bone volume that would be expected to resorb, remain unchanged, or remodel based on the strain energy density changes between the implanted and intact models. In their conclusions, central implants presented the best performance as those implants produced the least simulated resorbing potential in cortical and trabecular bone, with boundary-crossing implants having the highest simulated trabecular remodelling potentials. The results obtained in this

work cannot be directly compared with those obtained by Reeves et al. (2018) because, first, they simulated a potential bone response at the stage immediately after surgery instead of effectively simulating an iterative bone remodelling process, and second, there are no identical implants' geometries in the 2 studies. The results obtained in this work show a great change in bone mass in the anterior superficial region, as well as relevant changes in the lateral superficial region, which is in agreement with the findings of Reeves et al. (2018), as well as the radiologic outcomes of stemless implants reported by Habermeyer et al. (2015) and Krukenberg et al. (2018), and a single-photon emission CT/CT by Berth et al. (2015) who evaluated the local metabolic bone activity after a stemless shoulder arthroplasty. Moreover, Gallacher et al. (2018) reported radiolucencies lines beneath the trunion base plate of the Eclipse implant, stating that they could represent stress shielding, which was confirmed in this study. Recently, in a study about the bone remodelling process due to a Sidus Stem-Free Shoulder System, Santos et al. (2018) reported, through the computation of the change in bone mass, that the stemless model analysed showed bone resorption around the anchor, and bone apposition around the anchor edges and at the end of the anchor open-windowed fins. Quantitatively, the greatest bone mass loss occurred, superficially, in the anterior-superior and posterior-superior ROIs, while a moderated gain in bone mass occurred, deeply, in the posterior-superior ROI. The remaining ROIs showed bone mass loss within -3 % to -9 %. Despite some differences, which may be due to the different definition of the ROIs, the quantitative results obtained in this work for the Sidus implant are in accordance with those from Santos et al. (2018), as the greatest bone mass loss occurred, superficially, in the lateral and anterior ROIs, and a gain in bone mass was observed in the deep posterior ROI. Qualitatively, some local differences are observed compared to Santos et al. (2018). The averaging of the change in bone mass for each ROI hide some local effects which could explain these differences. In this work, a smaller amount of bone resorption is estimated in the superficial central region. In the lateral region, bone resorption around the implant's fins and less bone formation at the end of the implant's fins is observed. The differences observed between this study and that from Santos et al. (2018) are likely due to the differences in the loading conditions. This study considers not only the forces produced at the muscle attachment sites but also those due to the wrapping of muscles over the anatomical structures whereas Santos et al. (2018) only considered the forces at the muscle attachment sites.

Despite its contributions, the present work contains some limitations. First, only one humerus' geometry was studied. Even though it would have been valuable to have more than one humerus geometry, the dimensions of the humerus analysed fall within those of typical humeri, and thus the results are expected to be representative of humeri in general (Hertel et al., 2002). Regarding the loading conditions, the use of 6 load cases strengths the model. Yet, the addition of more load cases would allow a closer approximation to reality. In the remodelling simulations, the osseointegration process was not modelled. To evaluate the impact of this limitation, two extreme conditions for osseointegration were considered: an idealized condition of full osseointegration and a worst-case condition of absence of osseointegration. Even though quantitative differences were observed in the results due to the osteointegration conditions, no differences were observed qualitatively. The implants' models were not provided by the manufacturers, thus all the 5 prostheses were modelled according to the information available on the surgical technique guides or in the product's brochures. In other words, differences may exist between the modelled implants and the implants produced by the manufacturers. The significant variability in the geometry of the implants analysed prevented definite conclusions about some design features due to the absence of an identical implant only differing in one design feature. Nevertheless, the overall analysis could give an extensive insight about the performance of 5 commercialized stemless implants. The model was validated considering only its ability to reproduce the actual density distribution of the humerus. However, to provide further confidence on the results, further analyses were performed to evaluate the influence of the parameter k on the results. The sensitivity analysis performed showed that a change of 50 % in the parameter k did not change the findings of this study.

5. Conclusion

Overall, the geometry was shown to influence the bone adaption process of the humerus. From the bone remodelling point of view, the Global Icon, SMR, and Simpliciti implants showed a good performance, whereas the Eclipse implant had the worst performance, followed by the Sidus implant. However, the superior bone resorption level predicted for the Global Icon and Simpliciti models at the superficial central region of the implant's fixation might suggest a better long-term performance of the SMR, even regardless of the gain in bone mass predicted for the Simpliciti implant, because the bone loss observed for the former implants could lead to loosening over time (Quental et al., 2014a; Reeves et al., 2018). Although these findings may give indications to manufacturers and orthopaedic surgeons about the influence of the geometry in the bone adaptation process of the humerus, long-term clinical and radiological outcomes addressing more implants are essential to better understand the performance of stemless implants in the long-term

To the author's knowledge, this is the first study to perform such an extensive evaluation of the impact of the geometry of stemless implants, available in the market, on the bone adaption process of the humerus after a shoulder arthroplasty. Nonetheless, much work remains to be done.

References

Alidousti, H., Giles, J. W., Emery, R. J. H., & Jeffers, J. (2017). Spatial mapping of humeral head bone density. *Journal of Shoulder and Elbow Surgery*, *26*(9), 1653–1661.

Berth, A., März, V., Wissel, H., Awiszus, F., Amthauer, H., & Lohmann, C. H. (2015). SPECT/CT demonstrates the osseointegrative response of a stemless shoulder prosthesis. *Journal of Shoulder and Elbow Surgery*, *25*(4), e96–e103.

Berth, A., & Pap, G. (2013). Stemless shoulder prosthesis versus conventional anatomic shoulder prosthesis in patients with osteoarthritis. *Journal of Orthopaedics and Traumatology*, *14*(1), 31–37.

Churchill, R. S., & Athwal, G. S. (2016). Stemless shoulder arthroplasty—current results and designs. *Current Reviews in Musculoskeletal Medicine*, *9*(1), 10–16.

Churchill, R. S., Chuinard, C., Wiater, J. M., Friedman, R., Freehill, M., Jacobson, S., Nicholson, G. P. (2016). Clinical and radiographic outcomes of the simpliciti canal-sparing shoulder arthroplasty system. *Journal of Bone and Joint Surgery - American Volume*, *98*(7), 552–560.

Coley, B., Jolles, B. M., Farron, A., & Aminian, K. (2008). Arm position during daily activity. *Gait and Posture*, *28*(4), 581–587.

Coley, B., Jolles, B. M., Farron, A., & Aminian, K. (2009). Detection of the movement of the humerus during daily activity. *Medical and Biological Engineering and Computing*, *47*(5 SPEC. ISS.), 467–474.

Dassault Systèmes. (2015). Abaqus 2016 Online Documentation - Abaqus/CAE User's Guide. Retrieved August 25, 2018, from http://130.149.89.49:2080/v2016/index.html

Eberle, S., & Augat, P. (2007). Preventing Contact Convergence Problems in Bone- Implant Contact Models. *ANSYS Conference 25th CADHEM Users Meeting 2007*, 21–25.

Favre, P., & Henderson, A. D. (2016). Prediction of stemless humeral implant micromotion during upper limb activities. *Clinical Biomechanics*, *36*, 46–51.

Fernandes, P., Rodrigues, H., & Jacobs, C. (1999). A model of bone adaptation using a global optimisation criterion based on the trajectorial theory of wolff. *Computer Methods in Biomechanics and Biomedical Engineering*, *2*(2), 125–138.

Folgado, J. (2004). *Modelos Computacionais para Análise e Projecto de Próteses Ortopédicas*. Instituto Superior Técnico.

Folgado, J., Fernandes, P. R., Guedes, J. M., & Rodrigues, H. C. (2004). Evaluation of osteoporotic bone quality by a computational model for bone remodeling. *Computers & Structures*, *82*(17–19), 1381–1388.

Gallacher, S., Williams, H. L. M., King, A., Kitson, J., Smith, C. D., & Thomas, W. J. (2018). Clinical and radiologic outcomes following total shoulder arthroplasty using Arthrex Eclipse stemless humeral component with minimum 2 years' follow-up. *Journal of Shoulder and Elbow Surgery*.

Grant, J. A., Bishop, N. E., Götzen, N., Sprecher, C., Honl, M., & Morlock, M. M. (2007). Artificial composite bone as a model of human trabecular bone: The implant-bone interface. *Journal of Biomechanics*, *40*(5), 1158–1164.

Guedes, J., & Kikuchi, N. (1990). Preprocessing and postprocessing for materials based on the homogenization method with adaptive finite element methods. *Computer Methods In Applied Mechanics and Engineering*, *83*(2), 143–198.

Gupta, S., & Dan, P. (2004). Bone geometry and mechanical properties of the human scapula using computed tomography data, *17*(2), 61–70.

Habermeyer, P., Lichtenberg, S., Tauber, M., & Magosch, P. (2015). Midterm results of stemless shoulder arthroplasty: A prospective study. *Journal of Shoulder and Elbow Surgery*, *24*(9), 1463–1472.

Hawi, N., Magosch, P., Tauber, M., Lichtenberg, S., & Habermeyer, P. (2017). Nine-year outcome after anatomic stemless shoulder prosthesis: clinical and radiologic results. *Journal of Shoulder and Elbow Surgery*, *26*(9), 1609–1615.

Hertel, R., Knothe, U., & Ballmer, F. T. (2002). Geometry of the proximal humerus and implications for prosthetic design. *Journal of Shoulder and Elbow Surgery*, *11*(4), 331–338.

Heuberer, P. R., Brandl, G., Pauzenberger, L., Laky, B., Kriegleder, B., & Anderl, W. (2018). Radiological changes do not influence clinical mid-term outcome in stemless humeral head replacements with hollow screw fixation: a prospective radiological and clinical evaluation. *BMC Musculoskeletal Disorders*, *19*(1), 28.

Hogg, M. (2013). bonemapy 0.4.1 : Python Package Index. Retrieved April 20, 2018, from https://pypi.org/project/bonemapy/

Jacobs, C. R., Levenston, M. E., Beaupré, G. S., Simo, J. C., & Carter, D. R. (1995). Numerical instabilities in bone remodeling simulations: The advantages of a node-based finite element approach. *Journal of Biomechanics*, *28*(4), 449–459.

Krukenberg, A., McBirnie, J., Bartsch, S., Böhler, N., Wiedemann, E., Jost, B., Scheibel, M. (2018). Sidus Stem-Free Shoulder System for primary osteoarthritis: short-term results of a multicenter study. *Journal of Shoulder and Elbow Surgery*, *27*(8), 1483–1490.

Lima Corporate. (2016). SMR Stemless - Brochure, (c), 1–4.

Lübbeke, A., Rees, J. L., Barea, C., Combescure, C., Carr, A. J., & Silman, A. J. (2017). International variation in shoulder arthroplasty. *Acta Orthopaedica*, *88*(6), 592–599.

Magosch, P., Habermeyer, P., Bachmaier, S., & Metcalfe, N. (2012). Biomechanische Grundlagen des metaphysär verankerten Humeruskopfersatzes. *Obere Extremitat*, *7*(1), 11–16.

Nagels, J., Stokdijk, M., & Rozing, P. M. (2003). Stress shielding and bone resorption in shoulder arthroplasty. *Journal of Shoulder and Elbow Surgery*, *12*(1), 35–39.

Quental, C., Fernandes, P. R., Monteiro, J., & Folgado, J. (2014a). Bone remodelling of the scapula after a total shoulder arthroplasty. *Biomechanics and Modeling in Mechanobiology*, *13*(4), 827–838.

Quental, C., Folgado, J., Ambrósio, J., & Monteiro, J. (2012a). A multibody biomechanical model of the upper limb including the shoulder girdle. *Multibody System Dynamics*, *28*(1–2), 83–108.

Quental, C., Folgado, J., Fernandes, P. R., & Monteiro, J. (2012b). Bone remodelling analysis of the humerus after a shoulder arthroplasty. *Medical Engineering & Physics*, *34*(8), 1132–1138.

Quental, C., Folgado, J., Fernandes, P. R., & Monteiro, J. (2014b). Subject-specific bone remodelling of the scapula. *Computer Methods in Biomechanics and Biomedical Engineering*, *17*(10), 1129–1143.

Rancourt, D., & Drouin, G. (1990). Friction properties of the interface between porous-surfaced metals and tibia1 cancellous bone, *24*, 1503–1519.

Razfar, N., Reeves, J. M., Langohr, D. G., Willing, R., Athwal, G. S., & Johnson, J. A. (2015). Comparison of proximal humeral bone stresses between stemless, short stem, and standard stem length: a finite element analysis. *Journal of Shoulder and Elbow Surgery*, *25*(7), 1076–1083.

Reeves, J. M., Athwal, G. S., & Johnson, J. A. (2017). An assessment of proximal humerus density with reference to stemless implants. *Journal of Shoulder and Elbow Surgery*, *27*(4), 641–649.

Reeves, J. M., Langohr, G. D. G., Athwal, G. S., & Johnson, J. A. (2018). The effect of stemless humeral component fixation feature design on bone stress and strain response: a finite element analysis. *Journal of Shoulder and Elbow Surgery*.

Santos, B., Quental, C., Folgado, J., Sarmento, M., & Monteiro, J. (2018). Bone remodelling of the humerus after a resurfacing and a stemless shoulder arthroplasty. *Clinical Biomechanics*, *59*(8), 78–84.

Sobocinski, M. (2015). Analysis of biobearings friction and wear processes. *Journal of Applied Mathematics and Computational Mechanics*, *14*(2), 103–109.

Spitzer, V., Ackerman, M. J., Scherzinger, a L., & Whitlock, D. (1996). The Visible Human Male: A Technical Report. *Journal of the American Medical Informatics Association*, *3*(2), 118–130.

Swaminathan, V., & Gilbert, J. L. (2012). Fretting corrosion of CoCrMo and Ti6Al4V interfaces. *Biomaterials*, *33*(22), 5487–5503.